Earth and Planetary Science Letters 443 (2016) 153–161

Contents lists available at ScienceDirect

Earth and Planetary Science Letters

www.elsevier.com/locate/epsl

Geometrical evolution of interlocked rough slip surfaces: The role of normal stress

Nir Badt [a], Yossef H. Hatzor [a], Renaud Toussaint [b], Amir Sagy [c,*]

[a] Department of Geological and Environmental Science, Ben-Gurion University of the Negev, Beer Sheva 84105, Israel
[b] Institut de physique du globe de Strasbourg, 5, rue René Descartes, F-67084 Strasbourg cedex, France
[c] Geological Survey of Israel, 30 Malkhe Israel, Jerusalem 95501, Israel

ARTICLE INFO

Article history:
Received 13 November 2015
Received in revised form 6 March 2016
Accepted 12 March 2016
Available online xxxx
Editor: P. Shearer

Keywords:
roughness evolution
fault geometry
direct shear
mechanical work
wear
surface roughness

ABSTRACT

We study the evolution of slip surface topography using direct shear tests of perfectly mating surfaces. The tests are performed under imposed constant normal stress and constant slip rate conditions, to a sliding distance comparable to the roughness scale of the studied surfaces. Prismatic limestone blocks are fractured in tension using four-point bending and the generated surface topographies are measured using a laser profilometer. The initially rough fracture interfaces are tested in direct shear while ensuring a perfectly mating configuration at the beginning of each test. The predetermined sliding distance in all tests is 10 mm and the sliding velocity is 0.05 mm/s. A constant normal stress is maintained throughout the tests using closed loop servo control. The range of normal stresses applied is between 2 MPa and 15 MPa. After shearing, the surface topographies are re-scanned and the geometrical evolution is analyzed. We find that surface roughness increases with increasing normal stress: under normal stresses below 5 MPa the surfaces become smoother compared to the original geometry, whereas under normal stresses between 7.5 MPa and 15 MPa the surfaces clearly become rougher following shear. Statistical spectral analyses of the roughness profiles indicate that roughness increases with length-scale. Power spectral density values parallel to the slip orientation are fitted by power-law with typical power value of 2.6, corresponding to a Hurst exponent of 0.8, assuming self-affine roughness. This power value is consistent for the post-sheared surfaces and is obtained even when the original surface roughness does not follow initially a power-law form. The value of the scaling-law prefactor however increases with increasing normal stress. We find that the deformation associated with shearing initially rough interlocked surfaces extends beyond the immediate tested surface, further into the intact rock material. The intensity of the damage and its spatial distribution clearly increase with increasing normal stress. Wear loss is measured by subtracting the post-shear surface from the pre-shear surface matrices using known reference points. Our measurements indicate that wear loss and roughness evolution are both positively correlated with the mechanical shear work applied during the experiments. We argue, therefore, that normal stress plays a significant role in the evolution of interlocked surfaces, such as geological faults, and strongly affects the energy partitioning during slip.

1. Introduction

Faults in the upper crust are characterized by complex zones of deformed rock that shear during repeated faulting events (Chester and Logan, 1986; Ben-Zion and Sammis, 2003; Wibberley et al., 2008; Faulkner et al., 2010). Most of the displacement along faults is localized at principal slip surfaces exhibiting geometrical irregularity at all measurable scales (Power et al., 1988; Siman-Tov et al., 2013; Candela et al., 2012) and as in other material interfaces the roughness is critical to the understanding of shear and frictional processes (e.g. Bowden and Tabor, 1950; Dieterich and Kilgore, 1994). The presence of gouge and cataclasite zones in natural faults indicates that the fault surface itself evolves through wear production (Power et al., 1988; Wang and Scholz, 1994). In each slip event wear is generated and the initial geometry of the slip surface is continuously modified, a process that has been referred to as “roughness evolution” (Sagy et al., 2007).

Previous roughness evolution studies in the field by means of geometrical measurements of natural fault surfaces suggest that faults smooth with accumulated slip. Wesnousky (1988) observed strike-slip fault traces at geological map scales and discovered that

* Corresponding author.
E-mail address: asagy@gsi.gov.il (A. Sagy).

http://dx.doi.org/10.1016/j.epsl.2016.03.026
0012-821X/

the number of steps along the trace reduces with increased offset on the faults. By comparing profiles along slip surfaces that accommodated dozens to hundreds of meters of displacement to these which sheared less than a meter, Sagy et al. (2007) concluded that roughness parallel to slip orientation reduced due to slip at all measured scales. Brodsky et al. (2011) increased the sampling population and demonstrated that roughness of profiles at lengths of 0.5 to 1 m decreased very gradually as function of the slip amount. Bistacchi et al. (2011) studied paleo-seismic fault surfaces exhumed from seismogenic depths and demonstrated that similar geometrical evolution occurs at these depths.

Surface roughness of fractures was intensively investigated in laboratory experiments as an integral component of contact and shear mechanics (e.g. Bowden and Tabor, 1950; Archard, 1953). Many pioneering works in rock mechanics investigated roughness of faults and fractures in relation to mechanical strength and shear resistance (Patton, 1966; Barton, 1976; Byerlee, 1978). In the last decades, quantitative statistical analysis methods to describe surface geometry were proposed (e.g. Mandelbrot, 1983; Bouchaud et al., 1990; Grasselli et al., 2002) and some were applied to describe rock discontinuities. Amitrano and Schmittbuhl (2002) for example measured the geometry of shear fractures formed by triaxial shear tests and suggested that they exhibited self-affine power-law geometry with Hurst exponents (H) of 0.8 and 0.74 for profiles normal and parallel to the slip direction, respectively. Results obtained with rotary shear tests demonstrated slip rate effects on surface roughness (Fondriest et al., 2013; Boneh et al., 2014; Siman-Tov et al., 2015). These studies focused solely on the roughness characteristics after slip and therefore the actual roughness evolution through shear remained unresolved.

Roughness evolution studies require information about the surface geometry before and after shear displacement. For example, evolution of self-affine geometry, with increasing H as function of the slip amount, was reported for a smooth halite sample that was sheared on a coarse sandpaper substrate (Renard et al., 2012). Davidesko et al. (2014) sheared rough tensile limestone fractures with known initial roughness to increasing slip distances up to 15 mm. They demonstrated that when shearing under relatively low normal stress (2 MPa) surface roughness decreased with increasing displacement, compared to the original roughness.

Normal stress is fundamental in the theory of friction and wear (Bowden and Tabor, 1950; Archard, 1953; Byerlee, 1978) and therefore it is reasonable to assume that it also strongly affects damage and deformation in natural faults which typically yield under tectonic stresses of significant magnitudes. In the present study the effect of normal stress on roughness evolution is examined by means of direct shear experiments coupled with laser profilometer measurements before and after shear. The advantage of the combined mechanical–tribological methodology adopted here is that multi-scale mating surfaces are sheared relative to each other as they do in natural faults, and are mapped with high precision before and after deformation. Moreover, the direct shear system used here allows great control and measuring capabilities during shear displacement. The acquired roughness data is examined both statistically, using spectral analyses, and morphologically, using cross-sections and height maps of the surfaces.

2. Experimental procedure

The experiments consist of several stages: 1) rough tensile surfaces are created using four-point bending; 2) both surfaces are scanned with a laser profilometer; 3) direct shear experiments under constant normal stress to target displacement of 10 mm are performed while ensuring the sheared surfaces are perfectly mating before shearing begins; 4) re-scanning of both surfaces; 5) roughness analysis.

The experimental surfaces are generated from prismatic limestone beams. The starting material is a fine-grained limestone with an average grain diameter of ~0.4 mm, known locally as “Hebron Marble”. Young’s modulus of 57 GPa, Poisson’s ratio of 0.29 and uniaxial compressive strength of 5.54 and 5.83 were measured for similar samples in a previous work (Davidesko, 2013).

The four-point bending tests utilized the direct shear system with the shear load frame removed and the normal piston used to deliver the axial load (Fig. 1a). A vertical notch, a few centimeters long, was pre-cut to direct the propagation direction of the induced tensile fracture during bending (see Fig. 1a). The produced surfaces were typically 8 cm wide and approximately 11 cm long.

The uniqueness of the surfaces produced this way is that the roughness of one surface matches exactly the roughness of the other, thus enabling the surfaces to slide relative to one another from a completely mating configuration. Furthermore, the roughness of each set (two mating surfaces) is neither predetermined nor reproducible. The experimental fault surfaces in the present study, therefore, differ substantially from the surfaces used in routine friction studies, because they allow examination of multiscale asperity interlocking contacts (Fig. 2).

The experimental fault surfaces are sheared in a hydraulic, servo-controlled, direct shear system (Fig. 1c) to a constant distance of 10 mm at a rate of 0.05 mm/s, under imposed constant normal stress so that the tested interface is allowed to dilate vertically during shear. Normal load is delivered from the axial piston which connects to the top of the shear load frame using a centering pin. The lower shear box rolls on frictionless rollers that are placed between the shear box and the base platen (Fig. 1d).

The fractured interfaces are cast in the shear boxes using concrete in a completely mating configuration so that when initially loaded the interlocking contacts are fully preserved. The shear boxes are placed in the shear load frame which is connected to the horizontal shear piston (Fig. 1c). Six linear variable displacement transducers (LVDTs) are attached to metal plates on both flanks of the steel frames (Fig. 1d); four vertical transducers are used to measure dilation during shear, and two horizontal transducers are used to measure shear displacement. The LVDTs monitor the displacements very close to the sliding interface, thus allowing excellent control capabilities during testing because the shear displacement feedback to the closed-loop system is obtained from the outputs of the two horizontal shear transducers.

The topography of the tested interfaces is obtained by means of laser profilometer (Fig. 1b) and the data are used for roughness analysis. Both top and bottom surfaces are scanned before and after shear. Prior to scanning, the surfaces are cleaned of dust and moisture. Wear particles are removed from the post-shear surfaces using a soft brush and air pressure. The scans are performed parallel to the direction of shear (longitudinal direction of the samples) using a 75 mm lens with a sampling frequency of 10 mm^{-1} and 34.34 mm^{-1} in the longitudinal and transverse directions, respectively. The scans are used to map the entire surface in four parallel strips from which roughness analysis is performed. By comparing the results to higher resolution measurements in the same samples it is concluded that the accuracy of the measurements is robust in our samples for detecting power spectral density values for wavelengths above 0.2 mm. All pre-shear scans had post-shear counterpart scans that covered the same area for later roughness comparison. The acquired scans data are presented using surface matrices of heights.

3. Mechanical results

The mechanical results obtained from six direct shear experiments conducted in the present study and data from one experiment conducted by Davidesko et al. (2014) are presented in

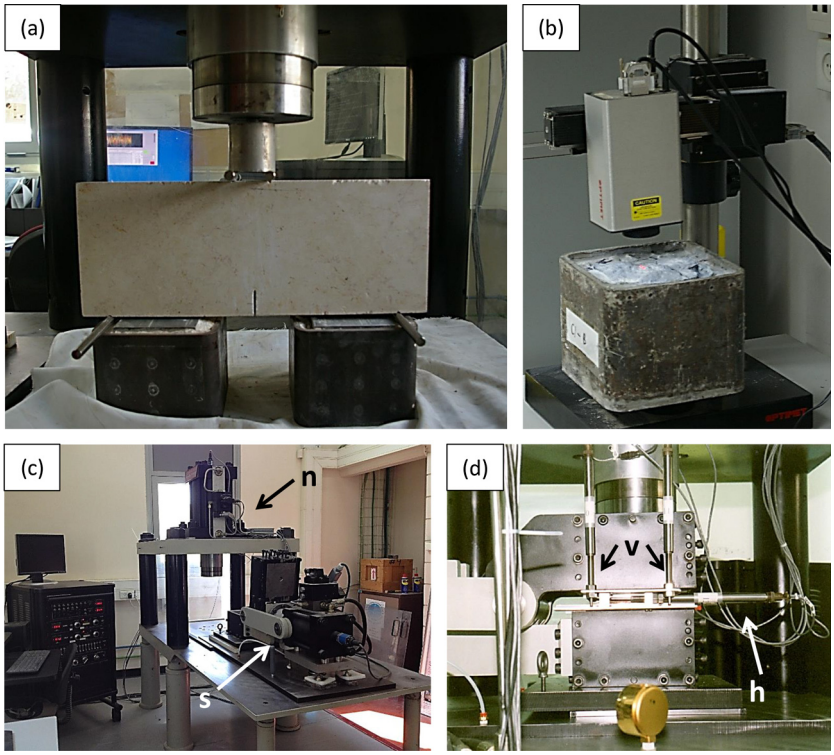

Fig. 1. Experimental methods in use: (a) Prismatic limestone beam in four-point bending configuration, the length of the beam is 50 cm long. (b) Profilometer scanning a surface, note that the surface is fixed to a steel shear box which links the sample to the direct shear system. (c) The direct shear system: the normal piston (delineated by *n* arrow) and the shear piston and load frame (delineated by *s* arrow). (d) Side view of the shear load frame with the vertical and horizontal LVDTs (delineated by *v* and *h* arrows, respectively).

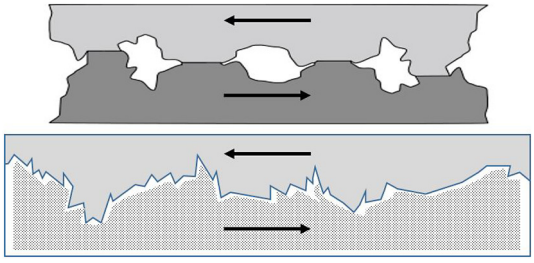

Fig. 2. Schematic illustration of tested surface configuration in typical rock friction and wear experiments (top) and the multi-scale, interlocking roughness in the present study (bottom).

Table 1 (Supplementary Material). All samples were sheared to a displacement of 10 mm at a rate of 0.05 mm/s under constant normal stress. During shear, dilation was allowed under the imposed normal stress boundary condition; an example of a typical stress-displacement curve is shown in Fig. 3. The results shown in Table 1 include measured shear (τ) and normal (σ_n) stress, calculated shear resistance (τ/σ_n), and calculated stress-drop ($\Delta\tau$). Shear resistance, as used here, is the value of the measured shear stress divided by the applied normal stress at any particular instance. Stress-drop refers to the change in shear stress from peak to minimum residual stress. It should be noted that while peak shear stress was clearly exhibited in all tests, a constant residual shear stress, elsewhere referred to as "steady state" friction (e.g. Dieterich and Kilgore, 1994) was never reached for the prespecified target displacement of 10 mm. We therefore use the tail of the shear stress–shear displacement curve to assign a residual shear stress value, thus obtaining the calculated stress-drop values reported in Table 1.

Peak shear stress was typically reached after a few millimeters (2–6) of displacement (Fig. 3a). Until that stage, the rough surfaces exhibited characteristic slip-hardening behavior attributed to elastic deformation and yield of asperities before peak shear stress is attained. As can be readily observed from inspection of Fig. 3(b), this stage was coupled with complex dilatational behavior, typically beginning with interface closure followed by interface opening, before peak shear stress is reached.

Maximum values of shear resistance did not correlate with the level of the imposed normal stress in our experiments. The maximum shear resistance here ($\tau/\sigma_n = 1.25$) was obtained by Davidesko et al. (2014), in a test which was performed under the lowest level of normal stress in this suite of tests, $\sigma_n = 2$ MPa. The minimum shear resistance ($\tau/\sigma_n = 0.661$) was measured in experiment LN6 performed under normal stress of $\sigma_n = 10$ MPa. This experiment is different from the rest because a precursory slip event occurred before peak stress was reached. The same phenomenon also occurred in experiment LN7 ($\sigma_n = 15$ MPa) where a significant stress-drop ($\sim$0.54 MPa) was registered before peak strength was attained. These precursory stress-drop events smoothed the stress-displacement curve, most likely dissipating some of the stored elastic energy prior to peak stress and consequent plastic yield of the tested interfaces. Due to the initially rough geometry of the surfaces, these precursory, uncontrolled events came as no surprise.

4. Geometrical evolution

Roughness topography of sheared surfaces typically evolves through wear production (Power et al., 1988; Wang and Scholz, 1994; Brodsky et al., 2011). Here we first present direct observations of geometrical variations followed by the statistical analysis of surface roughness. To prevent edge effects due to irregular fracturing at surface ends roughness analysis was performed on selected zones in the center of the samples, typically tens of millimeters long and 10–15 mm wide. The geometrical analyses, therefore,

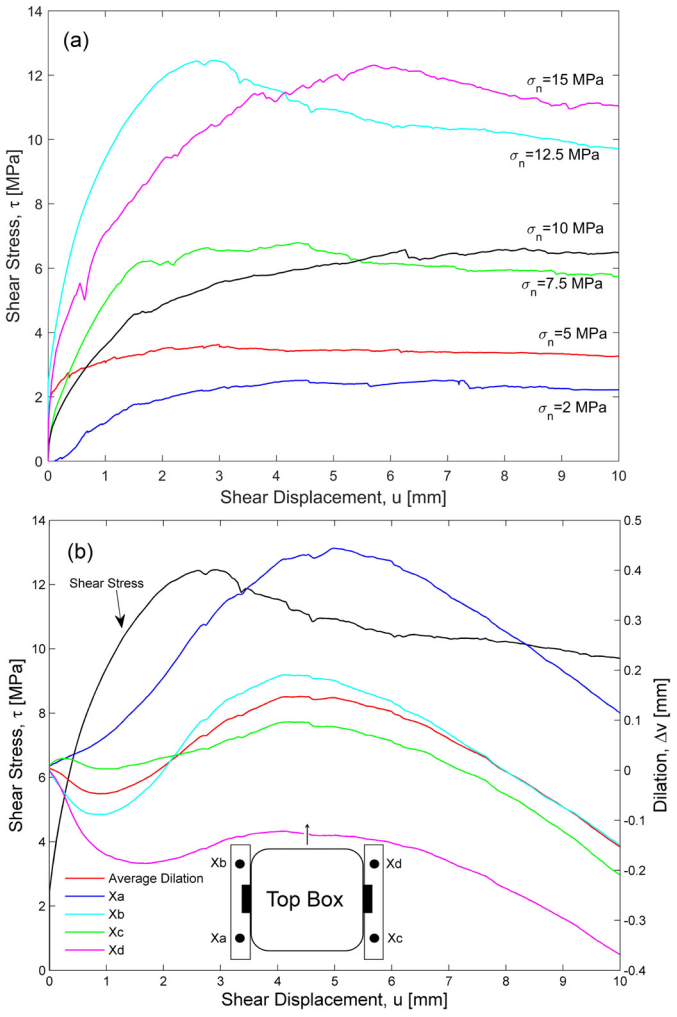

Fig. 3. (a) Shear stress–shear displacement curves for all experiments. (b) Experiment LN11, sheared under a normal stress of 12.5 MPa. Shear stress denoted by the black curve. The colored curves depict the dilation-displacement curves of all four vertical LVDTs (labeled Xa–Xd) and the average dilation (red curve). Note that here dilation is positive and contraction is negative. Schematic illustration of LVDT layout (horizontal, labeled Ya–Yb, and vertical, labeled Xa–Xd) presented in inset, shear direction marked by arrow. (For interpretation of the references to color in this figure legend, the reader is referred to the web version of this article.)

represent these zones specifically. The quantitative product for any given sample is a topographical map (expressed as a matrix) of any particular domain before and after shear. Fig. 4 displays topographical maps of surfaces before and after slip, obtained from two different experiments. Both surfaces evolved through shear, but under normal stress of $\sigma_n = 5$ MPa (Fig. 4a–b) the surface smoothed whereas under normal stress of 12.5 MPa (Fig. 4c–d) the surface became rougher. Similar roughening is also clearly observed in other surface maps of samples sheared under 7.5 and 15 MPa (see supplementary material). The topographical variations are demonstrated along two profiles parallel to the slip direction (Figs. 4b, d). It appears that the profiles in Fig. 4b suggest that under normal stress of 5 MPa the surfaces smoothed, most likely through asperity decapitation (Wang and Scholz, 1994), which decreased the overall roughness of the surface (see also Davidesko et al., 2014).

In contrast to the smoothing mechanism observed up to normal stress of 5 MPa, the clearly observed surface roughening under higher normal stresses is novel and not trivial to explain. We suggest that because the surfaces are initially rough and perfectly mating (Fig. 2) under higher normal stresses shear must be associated with significant penetrative damage. This process is best understood when the sheared surface morphology is carefully examined. Fig. 5 presents the surface of the sample that was sheared under normal stress of 12.5 MPa. Three main features can be identified across the surface. First, there are undamaged zones where the original texture is exposed. Other parts of the surface are covered by smooth grooves oriented in the slip direction, similar to slip striations observed on natural faults. The third distinctive features are fractures that penetrate into the shear interface to a depth of a few millimeters. The fracture intensity varies across the surface, with increasing density and penetration depth near geometrical irregularities. These fractures (Fig. 5b) resemble Riedel shears and tensile fractures which typically develop along natural faults (Tchalenko, 1968; De Paola et al., 2008). We find that such penetrative damage is much more significant in surfaces sheared under relatively higher normal stresses. Nonetheless, islands of striated polished zones (Figs. 5a, c) suggest simultaneous localization processes.

Statistical description of roughness evolution is performed using power spectral density (PSD) analysis, which provides quantitative roughness values and variations as a function of length scale. The analyses are performed on both pre- and post-shear matrices that contain the selected damage zones, on profiles parallel to the slip direction. The analysis follows a procedure introduced previously (Sagy and Brodsky, 2009; Brodsky et al., 2011; Candela et al., 2012; Davidesko et al., 2014); namely, any profile is de-trended and the discrete Fourier transform is calculated. The power is the square of the amplitudes of the coefficients and the PSD is the power spectrum normalized by the profile length. The PSD value, presented here for any given wavelength (Fig. 6), is averaged from the values calculated from several hundred profiles.

Fig. 6 presents power spectral densities as function of the length scale of experimental surfaces before (blue curves) and after (red curves) 10 mm of shear displacement under various normal stress levels. Interestingly, the initial roughness in part of the samples does not fit well one power-law and at relatively short wavelengths becomes moderate when compared to longer wavelengths (Fig. 6). However, the post-shear PSD curves closely fit a power of $\beta = 2.6$, or $H = 0.8$ (black lines).

Fig. 6 also shows that when the surfaces are sheared under normal stresses greater than 5 MPa the PSD increases at all measurable scales. The increase in PSD values corresponds to a mean increase in roughness for all the profiles that make up the surface at the specified wavelength. This behavior is clearly depicted in Fig. 7 where the PSD post to pre shear ratios are plotted as a function of the tested wavelength (final PSD(λ)/initial PSD(λ)). There is a distinct separation between samples sheared under normal stress levels greater than 5 MPa, all of which exhibit roughness ratios greater than 1 (roughening), and samples sheared under stress levels equal to or lower than 5 MPa, all of which exhibit roughness ratios smaller than 1 (smoothing). The above observations (Figs. 4–7) suggest that penetrative brittle fracturing is enhanced with increasing normal stress. During shear sliding, fragmentation occurs in and near the fractured zone and consequently rock fragments are detached from the host rock. Measurements of the surface irregularities indicate that roughness evolution reflects this wear mechanism.

5. Discussion

5.1. Geometrical–mechanical interactions

While this study focuses on roughness evolution, wear loss due to shear is a natural by-product of the geometrical evolution and is therefore examined as well. Wear loss is measured here by subtracting the post-shear from the pre-shear matrices, thus

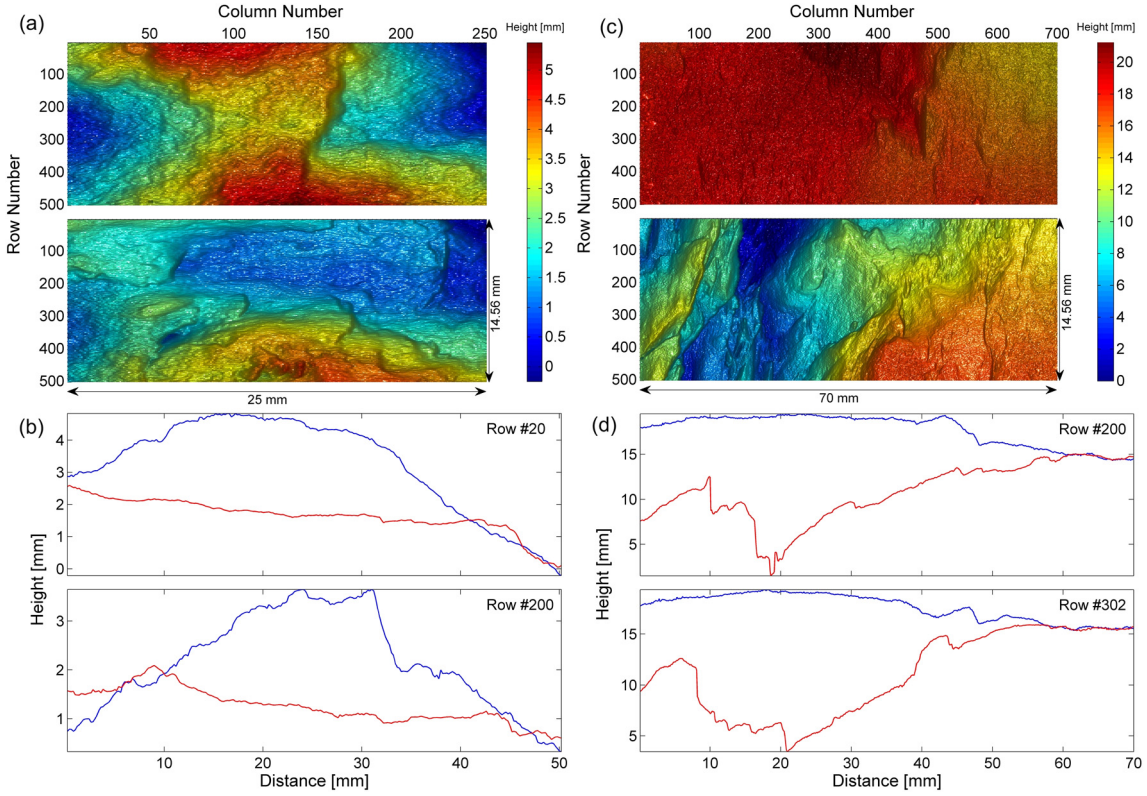

Fig. 4. Geometrical evolution of surfaces sheared under a normal stress of 5 MPa (a–b) and 12.5 MPa (c–d). (a, c) Pre-shear (top) and post-shear (bottom) matrices for surfaces sheared under $\sigma_n = 5$ MPa and $\sigma_n = 12.5$ MPa, respectively. (b, d) Selected profiles in direction parallel to shear (shear direction is to the left) for a surface sheared under $\sigma_n = 5$ MPa and $\sigma_n = 12.5$ MPa, respectively. The pre- and post-shear surfaces are depicted by blue and red curves, respectively. The matrices cover an area of 25×14.56 mm^2 and 69.9×14.56 mm^2 for the surface sheared under 5 MPa (a) and the surface sheared under 12.5 MPa (c), respectively. (For interpretation of the references to color in this figure legend, the reader is referred to the web version of this article.)

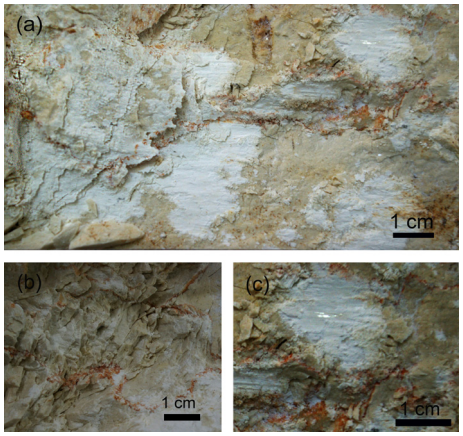

Fig. 5. Picture of a surface sheared under 12.5 MPa (a). Three different zones are identified; undamaged zones exhibiting the original texture of the rock, penetrative damage, exhibiting multiple fracture traces (b), and scattered zones of fine white gouge with slip-striations. Some of these contain highly polished patches (c).

delineating zones that experienced significant damage when interpreting the resulting height-difference matrix, referred to here as the "damage matrix" (Fig. 8). Such height subtraction was possible because some parts of the post-shear surface remained intact and could therefore be used as datum. Quantitative wear analysis is done by calculating the height difference between corresponding points in the pre- and post-shear matrices. Each point in the damage matrices represents a unit cell area of 0.1×0.0291 mm^2, corresponding to the resolution of the scan in both transverse and longitudinal directions, so that for each cell area we could calculate the wear volume at a good approximation. A threshold height difference is set to 0.5 mm in order to minimize height difference

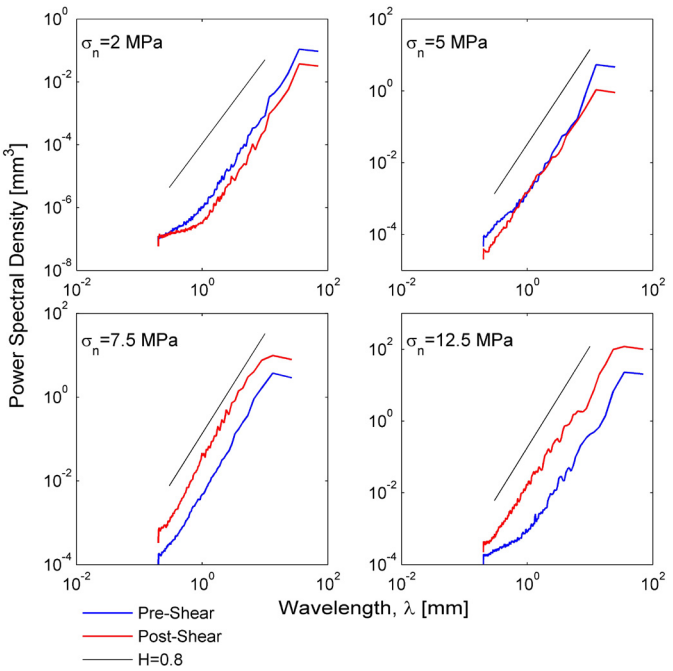

Fig. 6. Power spectral density roughness before (blue curves) and after (red curves) 10 mm shear under varying normal stresses. The slope in this bilogarithmic plot is of $\beta = 2.6$, corresponding to a Hurst exponent: $H = (\beta - 1)/2 = 0.8$. (For interpretation of the references to color in this figure legend, the reader is referred to the web version of this article.)

incompatibility of the pre- and post-shear matrices. The wear volume is normalized by the area of the whole damage matrix (or damage zone) as follows:

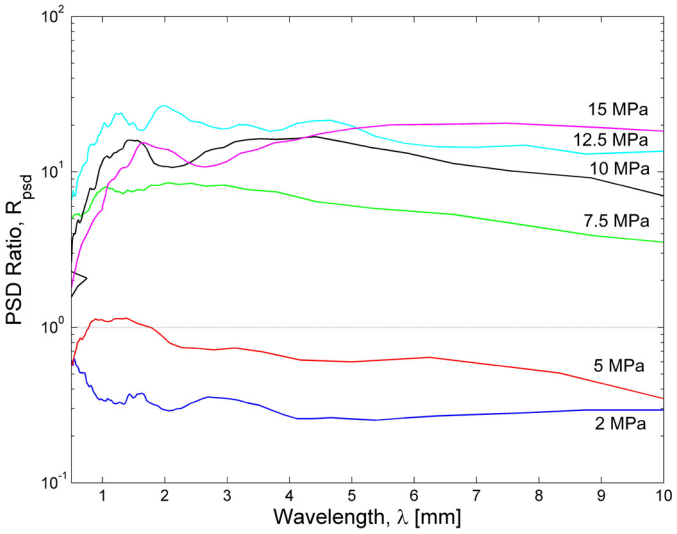

Fig. 7. Roughness evolution (PSD Ratio) as a function of wavelength for surfaces sheared under constant normal stress.

$$h_{wear} = \frac{\sum V_{ij}}{nA} \tag{1}$$

Where $\sum V_{ij}$ is the total wear volume obtained from all the unit cells in the matrix (above threshold value), n is the total number of cells in the entire matrix with height difference greater than the set threshold, and A is the unit cell area. The calculated wear volume is normalized by the area of the sampled zone. Combining measurements from both surfaces in a given experiment provides the average wear, expressed here in terms of total wear loss volume per damage area (Fig. 9a). Note that the average wear loss for the experiment sheared under 2 MPa (Fig. 9a, gray diamond) was calculated from only one surface; the wear volume per damage zone area was evaluated for that experiment by multiplying the original value by two. The main parameter that changed between experiments was the normal stress, but because the initial roughness of our samples although similar, was not identical, we plot the wear loss against the total mechanical shear work spent during the shearing process (Fig. 9), thus integrating the effects of normal stress, surface geometry, and material properties. The shear work due to shear sliding is obtained directly from the shear stress–shear displacement curves (e.g. Fig. 3):

$$W_t = \int_0^{10} \tau du \tag{2}$$

where W_t is the spent shear work during sliding to a pre-specified target distance of 10 mm, τ is the shear stress and du is the displacement interval.

The relationships between mechanical shear work (normalized by surface area) and wear loss, normal stress, and roughness ratio are plotted (Fig. 9), where the roughness ratio is defined as the PSD's ratio along the range of 1 mm to 1 cm. As would be intuitively expected, shear induced wear generation and surface roughening are energy sinks, requiring increasing amounts of mechanical energy to be provided by the loading system as shear deformation progresses.

5.2. Roughness evolution

The quantitative PSD analyses performed on the experimental slip surfaces portray the geometrical modification of the surfaces through shear. The overall picture suggests that surface roughness increases through shear under relatively high normal stresses

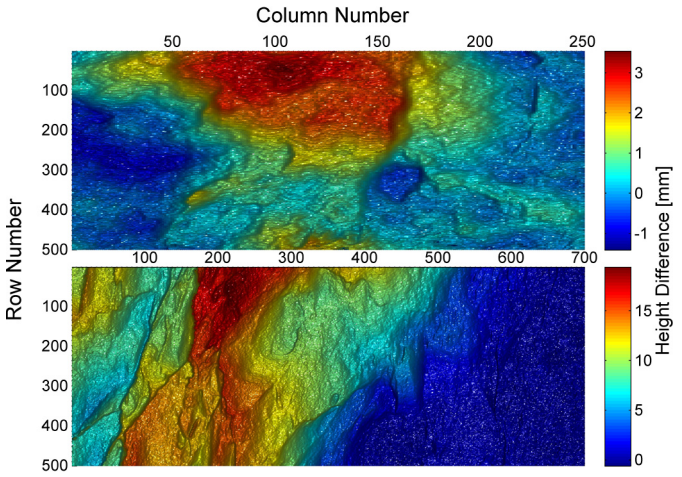

Fig. 8. Damage matrices for surfaces that were sheared under 5 MPa (top) and 12.5 MPa (bottom). The matrices depict zones that underwent significant damage (red areas) and undamaged zones (blue areas) that were used as reference for "zeroing" the pre- and post-shear matrices. (For interpretation of the references to color in this figure legend, the reader is referred to the web version of this article.)

(≥7.5 MPa) and decreases under relatively low normal stresses (≤5 MPa). Previous experimental observations demonstrated that surface roughness smooths as function of slip distance (Davidesko et al., 2014). In those experiments, surface roughness of tensile fractures were fitted well by a similar power-law, before and after shear, suggesting that when a constant normal stress is applied during shear displacement the power spectral density of the surface can be described by:

$$p(\lambda) = k_{(d)}\lambda^{\beta} \tag{3}$$

where β is the slope of the PSD line (in logarithmic space) and $k_{(d)}$ is the slip dependent coefficient of the smoothing process. It is demonstrated here that when the amount of displacement is fixed and the normal stress varies, the PSD function can be described by:

$$p(\lambda) = k_{(N)}\lambda^{\beta} \tag{4}$$

where $k_{(N)}$ is the normal stress dependent coefficient of the roughening process. The prefactor k is therefore the parameter that varies most in our shear experiments. Interestingly, computer simulations demonstrated that the prefactor of the self-affine surface roughness is the main component of roughness that affects energy dissipation during faulting (Newman and Griffith, 2014).

On the other hand, in most sheared surfaces of both sets of experiments, the power β exhibits a typical value of 2.6, in direction of slip at the measured scales, which in self-affine surfaces corresponds to a roughness (or Hurst) exponent of H = 0.8, as measured in previous studies (Bouchaud, 1997), where $\beta = 1 + 2H$ (Barabási and Stanley, 1995). It is therefore suggested that this roughness exponent might represent a more general multiscale self-affine roughness as suggested previously both for tensile as well as shear fractures (e.g. Bouchaud et al., 1990; Amitrano and Schmittbuhl, 2002; Renard et al., 2006).

Examination of the experimental surfaces more locally reveals that the tested surfaces undergo smoothing and roughening at different localities (Fig. 10a). The pre- and post-shear curves display an overall increase in surface roughness; however, when different zones in the same post-shear surface matrix are examined, areas of different roughness characteristics are evident. The rough zone (magenta colored curve) exhibits the maximum PSD values for each wavelength. In contrast, the smooth zone showing striations with no intensive penetrative damage, exhibits PSD values that are much closer to the initial values before slip has occurred. When

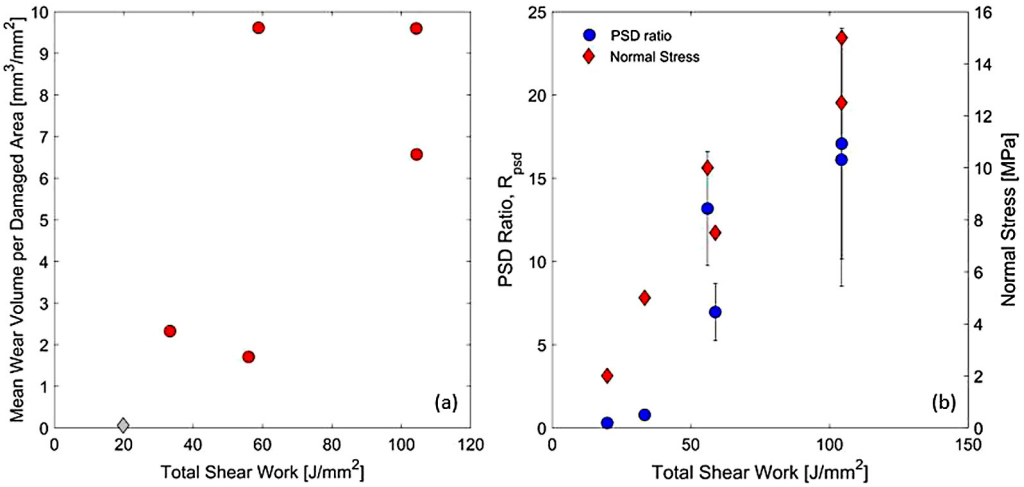

Fig. 9. Wear loss and roughness ratio presented against the total shear work. The average width of the wear volume in any given sample is presented in Fig. 9a. Red dots represent values calculated using measurements from both mating surfaces, while the grey diamond represents a value obtained from a single surface and multiplied by two. PSD ratio and normal stress values are presented in Fig. 9b. The error bars (right) depict one standard deviation. (For interpretation of the references to color in this figure legend, the reader is referred to the web version of this article.)

two PSD functions with equal power ($\beta = 2.6$) but different prefactor values are plotted along with the surface data, it can be concluded that while some variations in the power exist in the data, the predominant change in roughness is manifested mathematically as an increase or decrease in the prefactor (k) value. Following our observation that the prefactor is normal-stress-dependent, and its value increases with normal stress (Figs. 6–7), we conclude that the same process also occurs locally. The striation zones have presumably experienced a lower level of local normal stress than the rough ones. These local variations of normal stress are mostly influenced by the initial geometry of the fault, as evident by direct observations (Fig. 5) and suggested by models of stress distribution near rough fault surfaces (Chester and Chester, 2000; Sagy and Brodsky, 2009; Griffith et al., 2010). We thus conclude that initial roughness strongly influences post slip damage intensity and surface geometry.

Figs. 6 and 10a also demonstrate that at short length scales (<1 mm) some of the initial tensile fracture surfaces display a kink in the PSD values. Examination of thin sections reveals that the average grain size of the tested rock before shear is 0.4 mm, and therefore the bend in the PSD values is best interpreted as associated with the typical grain scale of the samples ($\sim$1–0.1 mm). Such small-scale cutoff is commonly observed in tensile fractures for numerous materials (Bouchaud, 1997). Interestingly, this cutoff remains in post-shear PSD curves for the surface sheared under 2 MPa (Fig. 6), but diminishes in surfaces sheared under higher normal stresses (Figs. 6, 10a). Fig. 10b presents the most extreme case of deviation of initial roughness from a power-law. The plot includes measurements from the high resolution lens of 50 mm, which enlarges the scanning resolution down to less than 20 μm. The kink in the pre-shearing roughness is reduced in the post-shear roughness and "moves" around smaller wavelengths. This is attributed to higher efficiency of fragmentation in the grain scale during shear, as the grains themselves are fractured. The typical grain size in the gouge becomes smaller as shear progresses, as observed in Fig. 5 and discussed by Amitrano and Schmittbuhl (2002).

5.3. Implications to natural faulting processes

The initial setup presented here is of a tensile fracture that is reactivated by shear. Such a slip mode is common in natural environments (Segall and Pollard, 1983; Martel et al., 1988; Di Toro and Pennacchioni, 2005). Moreover, field and experimental observations as well as theoretical analyses demonstrate that the initial inelastic deformation of brittle rocks, even under compression, usually includes tensile mode fracturing, while shear occurs only when these fractures interact (Segall and Pollard, 1983; Ashby and Sammis, 1990; Reches and Lockner, 1994). More broadly, one can interpret our experimental setting as a simplification of the complex shear process across multiscale interlocked rough faults. At large scales, even mature faults can exhibit significant roughness (Wang and Bilek, 2011).

Friction experiments under constant normal loading conditions display in some configurations strain hardening and strain weakening stages, followed by low resistance to shear (e.g. Ohnaka, 2003). Considering previous (Davidesko et al., 2014) and current results, we suggest that the evolution of roughness in sheared interlocked surfaces exhibits a roughening stage during strain hardening while gradual localization and smoothing occurs during strain, or slip, weakening. Our samples which contained initially rough surfaces never experienced the entire transient stage because the displacement length required for crossing the entire transient stage is strongly dependent upon the initial roughness and the normal stress (Queener et al., 1965; Wang and Scholz, 1994). Fig. 10b demonstrates surface roughness in an experiment that was terminated during the slip weakening stage after 10 mm of slip. Although on average the surface roughened, smooth striated zones were observed (Fig. 5) indicating that some localization had already occurred. We therefore suggest that our experiments best simulate the deformation of a fault patch with roughness larger or comparable to the slip displacement of the event.

Contrary to this, many experimental works adopted the shearing of relatively smooth surfaces in order to study the friction properties of rocks. Unsurprisingly, the transient stage in these experiments is relatively short. Beyond this stage, under constant applied velocity and normal stress, roughness, wear rate and resistance to shear remain statistically stable, (Archard, 1953; Boneh et al., 2014; Lyakhovsky et al., 2014). We therefore assume that these experiments best simulate fault patches which absorbed slip amounts larger than their length. We also note that slip velocity and normal stress further affect surface roughness at this stage (Boneh et al., 2013; Chen et al., 2013; Fondriest et al., 2013; Siman-Tov et al., 2015).

Finally, natural fault roughness values decrease with net slip (Sagy et al., 2007; Bistacchi et al., 2011), albeit very gradually (Brodsky et al., 2011). Normal stress variations, as presented here, could be important to this evolution. Roughness and wear loss in

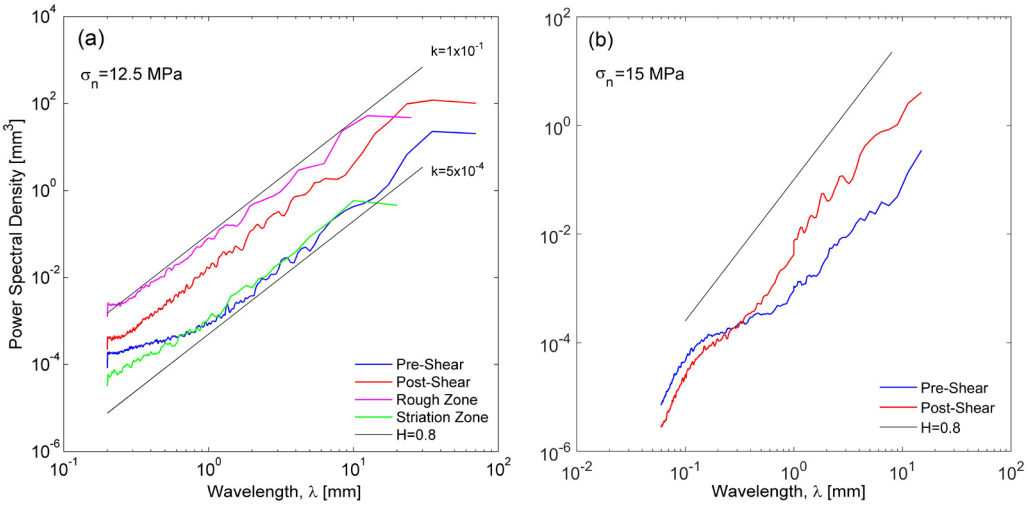

Fig. 10. (a) PSD curves for different zones of unequal roughness for a surface sheared under 12.5 MPa. The pre- and post-shear curves refer to the whole surface before and after shear, respectively. The rough and striation zone curves refer to two distinct zones in the post-shear surface that underwent roughening and smoothing, respectively. The two black solid lines are upper and lower bounds to the data featuring different values of k. (b) Power spectrum curves for a surface sheared under 15 MPa. Note the cross-over between the pre-shear (blue) and post-shear (red) curves around a wavelength of 0.4 mm. (For interpretation of the references to color in this figure legend, the reader is referred to the web version of this article.)

the present testing configuration evolve throughout brittle damage and increase with the mechanical shear work (Fig. 9). Following these results and previous theoretical analysis (Newman and Griffith, 2014) we speculate that the energy dissipation during natural slip is affected both by the level of normal stress and by the initial fault surface roughness. Further experimental and theoretical research focused on the transient wear stage is necessary for better simulating dissipation and partitioning of energy during earthquake.

6. Summary and conclusions

Our experimental configuration in which the surfaces are: a) initially rough, b) include multiscale geometrical irregularities, c) initially interlocked, and d) sheared to distances that are comparable to the roughness amplitude of the surface, is well suited for simulating natural faulting processes. Such a testing configuration has never been attempted in previous experimental shear and roughness evolution studies. While it is generally assumed that shearing surfaces one against the other is closely associated with polishing and smoothing of surface asperities, we find that deformation associated with shearing extends beyond the immediate zone of the asperities and that this deformation becomes more intensive with increasing normal stress. We demonstrate here that roughness evolution is a complex mechanism that consists of simultaneous roughening and smoothing of a given surface. Roughening occurs as part of damage development during strain hardening stage while gradual localization and smoothing occur during strain weakening. Under constant stress, the final roughness profile depends upon the slip amount (Davidesko et al., 2014). When the slip distance and the loading velocity are constant, the surface becomes rougher with increasing normal stress. Consequently, the roughness of the surface after shear can be higher than the initial roughness, an experimental finding never reported before.

We show that roughness, as function of measured wavelength, fits a power-law with power value of $\beta \sim 2.6$, or Hurst exponent of $H \sim 0.8$, assuming characteristic self-affine topography parallel to the slip direction (Figs. 6 and 10). Interestingly, this power is stable in the sheared surfaces even when the initial roughness does not fit a power-law, indicating that this characteristic roughness is an attractor for the morphology developed under brittle shear. Therefore, continuous shear can enlarge the range of length scales which statistically obey power-law roughness. The final roughness of the surface, which depends on the initial geometry, the level of normal stress, and the imposed sliding distance, is expressed by the evolution of the scaling-law prefactor. This value increases with normal stress but decreases with continuous slip.

Acknowledgements

We thank Telemaco Tesei and W. Ashley Griffith for their insightful comments and constructive review which helped improve this manuscript. This study is funded by Israel Science Foundation grant No. 929/10 and by USIAS Fellowship 2015, University of Strasbourg, France.

Appendix A. Supplementary material

Supplementary material related to this article can be found online at http://dx.doi.org/10.1016/j.epsl.2016.03.026.

References

Amitrano, D., Schmittbuhl, J., 2002. Fracture roughness and gouge distribution of a granite shear band. J. Geophys. Res. 107 (B12), 1978–2012. http://dx.doi.org/10.1029/2002JB001761.
Archard, J.F., 1953. Contact and rubbing of flat surfaces. J. Appl. Phys. 24 (8), 981–988.
Ashby, M.F., Sammis, C.G., 1990. The damage mechanics of brittle solids in compression. Pure Appl. Geophys. 133, 489–521.
Barabási, A.L., Stanley, H.E., 1995. Fractal Concepts in Surface Growth. Cambridge University Press.
Barton, N., 1976. Rock mechanics review: the shear strength of rock and rock joints. Int. J. Rock Mech. Min. Sci. Geomech. Abstr. 13, 255–279.
Ben-Zion, Y., Sammis, C.G., 2003. Characterization of fault zones. Pure Appl. Geophys. 160 (3–4), 677–715.
Bistacchi, A., Griffith, W.A., Smith, S.A., Di Toro, G., Jones, R., Nielsen, S., 2011. Fault roughness at seismogenic depths from LIDAR and photogrammetric analysis. Pure Appl. Geophys. 168 (12), 2345–2363.
Boneh, Y., Sagy, A., Reches, Z., 2013. Frictional strength and wear-rate of carbonate faults during high-velocity, steady-state sliding. Earth Planet. Sci. Lett. 381, 127–137.
Boneh, Y., Chang, J., Lockner, D.A., Reches, Z., 2014. Fault evolution by transient processes of wear and friction. Pure Appl. Geophys. 171 (11), 3125–3141.
Bouchaud, E., Lapasset, G., Planès, J., 1990. Fractal dimension of fractured surfaces: a universal value? Europhys. Lett. 13 (1), 73.
Bouchaud, E., 1997. Scaling properties of cracks. J. Phys. Condens. Matter 9 (21), 4319.

Bowden, F.P., Tabor, D., 1950. The Friction and Lubrication of Solids. Oxford University Press, Oxford.
Brodsky, E.E., Gilchrist, J.J., Sagy, A., Collettini, C., 2011. Faults smooth gradually as a function of slip. Earth Planet. Sci. Lett. 302, 185–193.
Byerlee, J., 1978. Friction of rocks. Pure Appl. Geophys. 116, 615–626.
Candela, T., Renard, F., Klinger, Y., Mair, K., Schmittbuhl, J., Brodsky, E.E., 2012. Roughness of fault surface over nine decade of length scales. J. Geophys. Res. 117 (B8).
Chen, X., Madden, A.S., Bickmore, B.R., Reches, Z.E., 2013. Dynamic weakening by nanoscale smoothing during high-velocity fault slip. Geology 41 (7), 739–742.
Chester, F.M., Logan, J.M., 1986. Implications for mechanical properties of brittle faults from observations of the Punchbowl fault zone, California. Pure Appl. Geophys. 124, 79–106.
Chester, F.M., Chester, J.S., 2000. Stress and deformation along wavy frictional faults. J. Geophys. Res. 105 (B10), 23421–23430.
Davidesko, G., 2013. Evolution of surface roughness through shear. M.Sc. Thesis. Ben-Gurion University of the Negev, Beer-Sheva, Israel.
Davidesko, G., Sagy, A., Hatzor, Y.H., 2014. Evolution of slip surface roughness through shear. Geophys. Res. Lett. 41 (5), 1492–1498.
De Paola, N., Collettini, C., Faulkner, D.R., Trippetta, F., 2008. Fault zone architecture and deformation processes within evaporitic rocks in the upper crust. Tectonics 27 (4).
Dieterich, J.H., Kilgore, B.D., 1994. Direct observation of frictional contacts: new insights for state-dependent properties. Pure Appl. Geophys. 143 (1–3), 283–302.
Di Toro, G., Pennacchioni, G., 2005. Fault plane processes and mesoscopic structure of a strong-type seismogenic fault in tonalites (Adamello batholith, Southern Alps). Tectonophysics 402 (1), 55–80.
Faulkner, D.R., Jackson, C.A.L., Lunn, R.J., Schlische, R.W., Shipton, Z.K., Wibberley, C.A.J., Withjack, M.O., 2010. A review of recent developments concerning the structure, mechanics and fluid flow properties of fault zones. J. Struct. Geol. 32 (11), 1557–1575.
Fondriest, M., Smith, S.A., Candela, T., Nielsen, S.B., Mair, K., Di Toro, G., 2013. Mirror-like faults and power dissipation during earthquakes. Geology 41 (11), 1175–1178.
Grasselli, G., Wirth, J., Egger, P., 2002. Quantitative three-dimensional description of a rough surface and parameter evolution with shearing. Int. J. Rock Mech. Min. Sci. 39 (6), 789–800.
Griffith, W.A., Nielsen, S., Di Toro, G., Smith, S.A., 2010. Rough faults, distributed weakening, and off-fault deformation. J. Geophys. Res. 115, B08409. http://dx.doi.org/10.1029/2009JB006925.
Lyakhovsky, V., Sagy, A., Boneh, Y., Reches, Z., 2014. Fault wear by damage evolution during steady-state slip. Pure Appl. Geophys. 171 (11), 3143–3157.
Mandelbrot, B.B., 1983. The Fractal Geometry of Nature. W.H. Freeman and Company, New York. 495 pp.
Martel, S.J., Pollard, D.D., Segall, P., 1988. Development of simple strike-slip fault zones, Mount Abbot quadrangle, Sierra Nevada, California. Geol. Soc. Am. Bull. 100 (9), 1451–1465.
Newman, P.J., Griffith, W.A., 2014. The work budget of rough faults. Tectonophysics 636, 100–110.
Ohnaka, M., 2003. A constitutive scaling law and a unified comprehension for frictional slip failure, shear fracture of intact rock, and earthquake rupture. J. Geophys. Res. B2, 2080. http://dx.doi.org/10.1029/2000JB000123.
Patton, F., 1966. Multiple modes of shear failure in rock. In: Proc. 1st Congr. Int. Soc. Rock Mech., vol. 1. Lisbon, pp. 509–513.
Power, W.L., Tullis, T.E., Weeks, J.D., 1988. Roughness and wear during brittle faulting. J. Geophys. Res. 93, 15268–15278.
Queener, C.A., Smith, T.C., Mitchell, W.L., 1965. Transient wear of machine parts. Wear 8, 391–400.
Reches, Z.E., Lockner, D.A., 1994. Nucleation and growth of faults in brittle rocks. J. Geophys. Res. 99 (B9), 18159–18173.
Renard, F., Viosin, C., Marsan, D., Schmittbuhl, J., 2006. High resolution 3D laser scanner measurements of a strike-slip fault quantify its morphological anisotropy at all scales. Geophys. Res. Lett. 33. http://dx.doi.org/10.1029/2005GL025038.
Renard, F., Mair, K., Gundersen, O., 2012. Surface roughness evolution on experimentally simulated faults. J. Struct. Geol. 45, 101–112.
Sagy, A., Brodsky, E., 2009. Geometric and rheologic asperities in an exposed fault zone. J. Geophys. Res. 114, B02301. http://dx.doi.org/10.1029/2008JB005701.
Sagy, A., Brodsky, E., Axen, G.J., 2007. Evolution of fault-surface roughness with slip. Geology 35 (3), 283–286.
Segall, P., Pollard, D.D., 1983. Nucleation and growth of strike slip faults in granite. J. Geophys. Res., Solid Earth 88 (B1), 555–568.
Siman-Tov, S., Aharonov, E., Sagy, A., Emmanuel, S., 2013. Nanograins form carbonate fault mirrors. Geology 41 (6), 703–706.
Siman-Tov, S., Aharonov, E., Boneh, Y., Reches, Z., 2015. Fault mirrors along carbonate faults: formation and destruction during shear experiments. Earth Planet. Sci. Lett. 430, 367–376.
Tchalenko, J., 1968. The evolution of kink-bands and the development of compression textures in sheared clays. Tectonophysics 6, 159–174.
Wang, W., Scholz, C.H., 1994. Wear processes during frictional sliding of rock: a theoretical and experimental study. J. Geophys. Res. 99 (B4), 6789–6799.
Wang, K., Bilek, S.L., 2011. Do subducting seamounts generate or stop large earthquakes? Geology 39 (9), 819–822.
Wesnousky, S.G., 1988. Seismological and structural evolution of strike-slip faults. Nature 335, 340–342.
Wibberley, C.A.J., Yielding, G., Di Toro, G., 2008. Recent advances in the understanding of fault zone internal structure: a review. Geol. Soc. (Lond.) Spec. Publ. 299 (1), 5–33.